Yi Yang, Ching-Tai Ng, Andrei Kotousov
Second-order harmonic generation of Lamb wave in prestressed plates
Journal of Sound and Vibration, 2019; 460:114903-1-114903-12

Second-order harmonic generation of Lamb wave in prestressed plates

Yi Yang[1,*], Ching-Tai Ng[1,†], Andrei Kotousov[2,‡]

[1] School of Civil, Environmental & Mining Engineering, The University of Adelaide, SA 5005, Australia

[2] School of Mechanical Engineering, The University of Adelaide, SA 5005, Australia

Abstract

This paper investigates the second-order harmonics generation associated with propagation of Lamb wave in pre-stressed plates. The second-order harmonic phenomena appear in a weakly non-linear medium due to material and geometry nonlinearities. This study proposes finite element (FE) models to incorporate stress constitutive equations formulated by Murgnahan's strain energy function. The model is used to take into account the stress effect on second-order harmonic generation of Lamb wave propagation in weakly nonlinear media. The developed FE model is first validated against two-dimensional (2D) analytical solutions. A three-dimensional (3D) FE model is then developed and utilised to study more realistic problems, such as the rate of accumulation of the non-linear parameter β' at different wave propagation angles when the plate is subjected to a bi-axial stress and the effect of the applied stresses on second-order harmonic generation in a plate with a fatigue crack. The results demonstrate that the applied stresses can notably change the value of β' in different directions. The finding of this study can gain physical insight into the physical phenomenon of stress effect on second-order harmonic generation of Lamb wave. Thus, the current study opens an opportunity for the development of a new non-destructive stress evaluation technique for plate- and shell-like structural

* Email: yi.yang01@adelaide.edu.au
† Corresponding author: A/Prof Ching Tai Ng (alex.ng@adelaide.edu.au)
‡ Email: andrei.kotousov@adelaide.edu.au

components. Moreover, the new technique can be easily incorporated with existing guided wave based-SHM systems and provide information regarding the change of the stress conditions. Such additional information can significantly improve the structural life prognosis and reduce risk of failures.

Keywords: Second-order harmonic; material nonlinearity; prestressed plate; finite element simulation; stress effect

1. Introduction

The importance of Structural Health Monitoring (SHM) in engineering field is currently undisputed, and benefits of SHM systems have been discussed in many papers [1]-[4]. SHM systems based on ultrasonic guided waves, such as Rayleigh wave [5][6], Lamb wave [7],[8] and torsional wave [9]-[10], have attracted attention over the past two decades [12]-[14], and different damage detection techniques using linear guided wave were developed and deployed across many industries [15]-[17]. One of the main objectives of the SHM systems is to provide the information in a real time, which is required for structural life prognosis and maintenance scheduling. However, the efficiency of the SHM systems as well as structural life prognosis is significantly affected by changing environmental and operational conditions [18],[19], such as the ambient temperature and applied loading on structures. Therefore, it is important to incorporate the evaluation of these factors into the on-line monitoring systems in order to improve the operation and maintenance procedures of high-value assets.

1.1. Acoustoelastic effect of Lamb waves

Most studies on the acoustoelastic of Lamb waves focused on the linear features, such as change of the phase velocity with the magnitude of the applied stress. Gandhi *et al*. [20] conducted a comprehensive analysis of the acoustoelastic effect associated with Lamb wave propagation in plates subjected to bi-axial loading. However, this analysis only considered the first-order of the infinitesimal strain tensor. In a recent study by Mohabuth *et al*. [21], a general theory was developed, and the governing equations were derived for the propagation of small amplitude waves in a pre-stressed plate using the theory of incremental deformations superimposed on large deformations. They also extended the study to plates subjected to a bi-axial stress [22] and investigate the large acoustoelastic effect of Lamb wave propagation in an incompressible elastic plate. The correction to the phase velocity due to the applied stress was obtained to the second order in pre-strain/stress [23]. The dispersion of the finite amplitude Lamb waves was studied with a higher (or third)-order elastic theory by Packo *et al*. [24]. Yang *et al*. [25] investigate the effect of axial stress on guided wave propagation using a semi-analytical finite element method. They investigated the stress effect on phase and group velocity of guided wave.

1.2. Nonlinear guided wave

There are many phenomena associated with non-linear guided waves, which can be utilised for the damage and stress evaluation. These phenomena include the generation of higher-order harmonics [26]-[28] and sidebands [29],[30]. According to the recent review of Jhang [31], the non-linearity mainly arise from two sources, material non-linearity, and contact non-linearity due to presence of contact-type defects or damage. The generation of higher-order harmonics due to contact nonlinearity has been investigated experimentally for bulk waves [32], Rayleigh

waves [33]-[35] as well as for Lamb waves. A number of recent studies have also focused on different types of damage, such as delamination [36]-[38], fatigue cracks [39]-[41], debonding [42][43], and loosening bolted joints [44][45].

The material nonlinearity has been a subject of many theoretical and experimental studies [26],[46]-[48]. According to the work of Pruell *et al*. [49] and Kim [50], plastic deformations and fatigue damage can be a source of the material non-linearities, in addition to the intrinsic non-linearity due to the inter-atomic and molecular forces. Therefore, it is possible to evaluate the fatigue life and the accumulated plastic deformations based on the change of the non-linear characteristics of ultrasonic waves. This possibility was recently demonstrated experimentally by Hong *et al*. [51], who incorporated the intrinsic material non-linearity and contact non-linearity associated with fatigue cracks and developed a method for fatigue damage detection.

It has been demonstrated in several studies that the phase and group velocity matching, and non-zero power flux are required to ensure that the higher-order harmonics grow with the distance, and hence, it becomes detectible with piezoceramic transducer and other sensors. Most of the studies considered the generation of the second-order harmonic associated with the first order symmetric (S_1) – second-order symmetric (S_2) mode pairs of Lamb waves, which satisfy the aforementioned matching conditions. Müller *et al.* [52] identified that there are five mode types that satisfy the requirements for cumulative increase in second harmonic amplitude through an analytical study. An experimental study of second harmonic generation was also conducted by Matlack *et al.* [53]. The study investigated the efficiency of second harmonic accumulation with propagation distances using both symmetric and anti-symmetric wave mode pairs, which satisfy the aforementioned requirements. However, at the high frequency, there are many wave modes, which makes it difficult to extract the non-linear parameter, such the rate of accumulation of the second-order harmonic with the propagation distance. Moreover,

Lamb waves are normally excited using a finite frequency bandwidth. Because the S_1 and S_2 Lamb wave are highly dispersive at the matching condition frequencies, there is only a fraction of the excitation power feeds the second-order harmonic, which make the accurate measurements very challenging.

Wan *et al*. [48] found that the velocity change of the fundamental symmetric (S_0) mode of Lamb waves is quite small in low frequency region and the velocity matching conditions can be satisfied approximately. Therefore, the generation and growth of the second-order harmonic can also be observed over a certain propagation distance in low frequency ultrasonic range. The propagation distance is closely related to the difference of the phase velocities between the primary and second-order harmonic of Lamb waves. This study showed that the data processing becomes much easier when only one Lamb wave mode exists. Moreover, the excitation of S_0 can be easily generated by using a common dual-transducer excitation method [54].

1.3. Stress effect on higher harmonic generation of nonlinear guided wave

There were limited studies focused on investigating phenomena of higher-order harmonic generation due to stress effect in the literature. In one-dimensional (1D) waveguide, Nucera and Lanza di Scalea showed that the higher-order harmonic generation of guided wave can be used to monitor load levels of multi-wire strands [55]. In their study, the higher-order harmonics are generated due to the nonlinearity from inter-wire contact. In two-dimensional (2D) waveguide, Pau and Lanza di Scalea [56] investigated the effect of the applied stress on the generation of the second-order harmonic. They proposed an analytical model to investigate the nonlinear guided wave propagation in prestressed plates.

The existing theoretical studies on the generation of the second-order harmonic are typically very cumbersome and rest on adopting several crucial assumptions, such as plane

stress or plane strain conditions, which are difficult to reproduce in experiments. Therefore, the outcomes of these studies cannot be readily adopted for practical purposes.

To address this problem, the current study in this paper develops a three-dimensional (3D) FE model to gain fundamental understanding of the stress effect on the second-order harmonic of Lamb waves under more realistic conditions i.e. conditions, which can be relatively easy reproduced in the laboratory environment. The previous theoretical results are utilised to validate this model. This provides the confidence in the outcomes of the more realistic 3D analysis of the second-order harmonic generation.

The paper is structured as follows. Section 2 describes the constitutive equations based on the Murgnahan's strain energy function. Section 3 provides the details of the implementation of the constitutive equations using VUMAT subroutine in ABAQUS software package. In Section 4, the developed FE model is validated against analytical and numerical results obtained under 2D assumptions. Section 5 presents a comprehensive 3D FE study of the effect of the applied stresses on the rate of the accumulation of the second-order harmonic at different wave propagation angles. Section 6 extends the current study to further consider the prestressed plate with a fatigue crack. The main results and possible implementation of these results to the stress evaluation are discussed in Section 7.

2. Constitutive Equations

The definition of position for material particle in the reference and current configuration follows the definition of Mohabuth *et al*. [21][22], which are defined as $\boldsymbol{X}$ and $\boldsymbol{x}$, respectively. The deformation gradient **F** is defined as

$$\boldsymbol{F} = \frac{\partial \boldsymbol{x}}{\partial \boldsymbol{X}} \tag{1}$$

The Green-Lagrange strain tensor is given by:

$$\mathbf{E} = \frac{1}{2}(\mathbf{C} - \mathbf{I}) \tag{2}$$

where **I** is the identity tensor and **C** is the right Cauchy-Green deformation tensor, which is defined as:

$$\mathbf{C} = \mathbf{F}^{\mathrm{T}}\mathbf{F} = \mathbf{U}^{\mathbf{2}} \tag{3}$$

where **U** is the right stretch tensor.

The strain energy function according to Murnaghan [57] is written as:

$$\mathrm{W}(\mathbf{E}) = \frac{1}{2}(\lambda + 2\mu)i_1^2 - 2\mu i_2 + \frac{1}{3}(l + m)i_1^2 - 2mi_1i_2 + ni_3 \tag{4}$$

where λ and μ are the lamé elastic constants; *l*, *m* and *n* are the third-order elastic constants or Murgnahan's constant. $i_1 = \mathrm{tr}(\mathbf{E})$, $i_2 = \frac{1}{2}[i_1^2 - \mathrm{tr}(\mathbf{E})^2]$, $i_3 = \det(\mathbf{E})$, respectively, are strain invariants. The partial derivatives of **W** with respect to **E** give the second Piola-Kirchhoff (PK2) stress:

$$\mathbf{T} = \frac{\partial \mathrm{W}(\mathbf{E})}{\partial \mathbf{E}} \tag{5}$$

The relationship between Cauchy stress and PK2 stress is given by the following equation:

$$\boldsymbol{\sigma} = \mathrm{J}^{-1}\mathbf{F}\mathbf{T}\mathbf{F}^{\mathrm{T}} = \mathrm{J}^{-1}\mathbf{F}\frac{\partial \mathrm{W}(\mathbf{E})}{\partial \mathbf{E}}\mathbf{F}^{\mathrm{T}} \tag{6}$$

where $\mathrm{J} = \det(\mathbf{F})$.

3. Implementation the Constitutive Equations in Finite Element Simulation

In ABAQUS/Explicit, VUMAT subroutine is normally used to introduce the user-defined constitutive behaviour of the material. VUMAT utilises the Cauchy stress tensor in Green-Naghdi basis, which is given by

$$\widehat{\boldsymbol{\sigma}} = \mathbf{R}^{\mathrm{T}}\boldsymbol{\sigma}\mathbf{R} \tag{7}$$

where **R** is rotation tensor, and **R** is a proper orthogonal tensor, i.e., $\mathbf{R}^{-1} = \mathbf{R}^{\mathrm{T}}$. The relationship between **F**, **U** and **R** is given by

$$\mathbf{F} = \mathbf{R}\mathbf{U} \tag{8}$$

Using Equations (6) and (8), Equation (7) can be written as

$$\widehat{\boldsymbol{\sigma}} = \mathrm{J}^{-1}\mathbf{R}^{\mathrm{T}}\mathbf{F}\mathbf{T}\mathbf{F}^{\mathrm{T}}\mathbf{R} = \mathrm{J}^{-1}\mathbf{R}^{\mathrm{T}}\mathbf{R}\mathbf{U}\mathbf{T}\mathbf{U}^{\mathrm{T}}\mathbf{R}^{\mathrm{T}}\mathbf{R} = \mathrm{J}^{-1}\mathbf{U}\frac{\partial \mathrm{W}(\mathbf{E})}{\partial \mathbf{E}}\mathbf{U}^{\mathrm{T}} \tag{9}$$

Equation (9) provides the stress-strain relationship, which are programmed in the VUMAT subroutine. The stress in VUMAT must be updated with in accordance to this equation at the end $(t + \Delta t)$ of an integration step and stored in stressNew(i) variable. These calculations are based on the values of **F** and **U** given in the subroutine at the end of the previous step (t).

4. Numerical Validation

This section presents the outcomes of a validation study of the VUMAT subroutine and FE model as described in Section 2. It is validated against the theoretical results published by Wan *et al*. [48]. A two-dimensional (2D) plane strain model is created in ABAQUS/Explicit and constitutive equations are converted to the 2D plane strain case. Figure 1 shows the schematic diagram of the FE model, which is a 2 mm thick and 1000 mm long plate made by aluminium. The Lamb wave signal is excited at the left end of the plate, and the excitation signal represents

a sinusoidal tone burst pulse modulated by a Hanning window. The excitation signal is prescribed to the displacement at the nodal points. A fixed boundary condition is assigned to the right end of the plate, which does not affect the calculations within a certain time window. 6061-T6 and 7075-T651 aluminium alloys are considered in the study and the material properties of these alloys, including the third-order elastic constants, are given in Table 1.

Figure 1: Schematic diagram of 2D FE plate model in ABAQUS

Table 1. Material properties of 6061-T6 and 7075-T651

Material	ρ (kg/m^3)	λ (GPa)	μ (GPa)	l (GPa)	m (GPa)	n (GPa)
6061-T6	2704	50.3	25.9	-281.5	-339	-416
7075-T651	2810	52.3	26.9	-252.2	-325	-351.2

In the FE analysis, the element size is selected to ensure that there are at least 20 elements per wavelength, so that the accuracy of the simulations is not compromised. There are also eight elements in the thickness direction. Since the second-order harmonic generation is of interest, the element size is selected based on the wavelength of the second-order harmonic Lamb waves. The elements used in this study are 4-node bilinear plane strain quadrilateral elements with reduced integration (CPE4R).

4.1. Second-order harmonic accumulation with the propagation distance

The maximum propagation distance within which the displacement amplitude of the second-order harmonic increases [48]) is investigated. The excitation signals of 300 kHz and 400 kHz

corresponding to the fundamental symmetric mode (S_0) of Lamb waves are excited at the left end of the plate. The number of cycles of the wave signal is 18 and the excitation magnitude of the displacement is set at 5 μm. For the 300 kHz excitation frequency, the measurement points are taken at every 50 mm, and for 400 kHz excitation frequency the measurement points are at every 12.5 mm. Figure 2a show an example of the 300kHz wave signal measured at 200 mm away from the excitation area in the time-domain. Figure 2b show the signal in frequency-domain. There are peak at excitation frequency 300 kHz and second-order harmonic frequency 600 kHz. The amplitudes of the second-order harmonic for the two fundamental excitation frequencies, 600 kHz and 800 kHz, are extracted from the frequency-domain of the simulation results and plotted in Figure 3. The results show that the maximum propagation distance of the second-order harmonic Lamb wave at 600 kHz kHz and 800 kHz are 200 mm and 62.5 mm respectively, and the corresponding theoretical values are 220.02 mm and 69.51 mm, respectively [48].

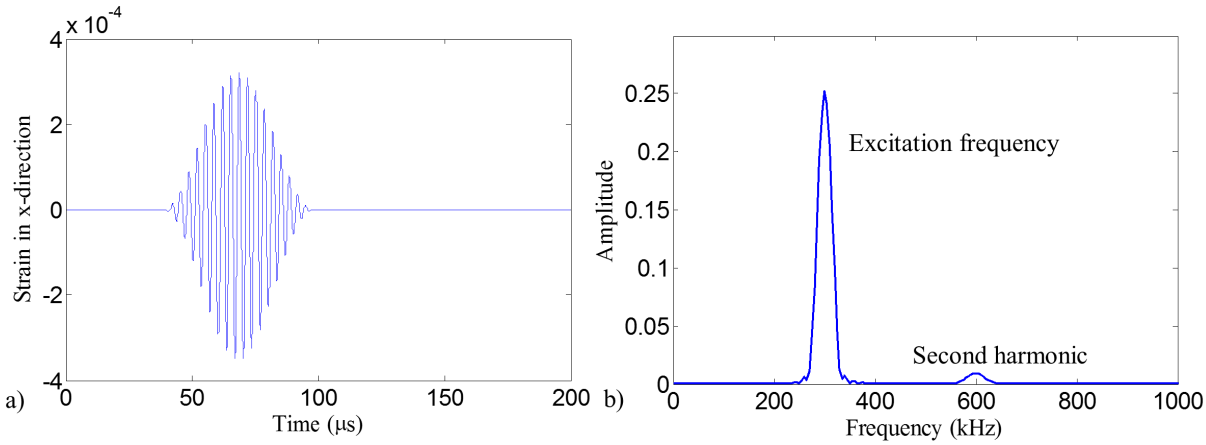

Figure 2: a) Time- and b) frequency- domain of strain in *x* direction calculated at 200 mm from the excitation location with 300kHz excitation signal

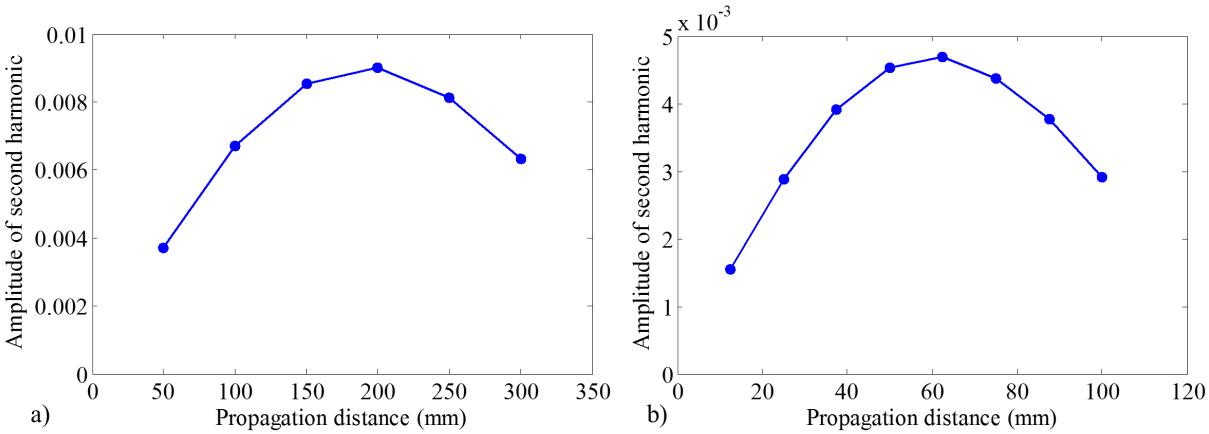

Figure 3: Second-order harmonic amplitude at a) 600 kHz and b) 800 kHz against propagation distance

4.2. Second-order harmonic accumulation of different materials

Another validation study is carried out to investigate the rate of accumulation (slope ratio) of the second-order harmonic generation with the propagation distances for the materials under consideration. The excitation frequency in this validation study is set at 100 kHz, and the second-order harmonic amplitude at 200 kHz keeps increasing until the propagation distance reaches 7764.7 mm [48]. The number of cycles of the excitation signal remains the same as in the previous study, i.e. 18 cycles. Numerical studies of the fundamental S_0 Lamb wave mode propagation are conducted using 6061-T6 and 7075-T651 aluminium alloys.

In this study, a non-linear parameter, β', is defined as a function of the propagation distance:

$$\beta' = \frac{A_2}{A_1^2} \tag{10}$$

where A_1 and A_2 are the amplitudes of the primary (excitation frequency) and the second-order harmonic, respectively, in frequency-domain at some certain distance from the excitation location. The magnitudes of the nonlinear parameter versus the propagation distance for the

two cases of material properties specified in Table 1 are shown in Figure 4. The third-order constants, l, m and n, of 6061-T6 aluminium alloy are larger than those of 7075-T651. The larger values of the third-order constants lead to larger values of the non-linear parameter and a higher rate of the accumulation of the amplitude of the non-linear parameter with the propagation distance. The slope of for the curve for 6061-T6 material properties is 0.00228 (mm^{-1}), while for the 7075-T651 alloy the slope is 0.00205 (mm^{-1}). As a result, the ratio between these two slopes is around 1.11, compared to the theoretical value of 1.12 [48]. The results show that there is good agreement between the theoretical and numerical result for all validation studies.

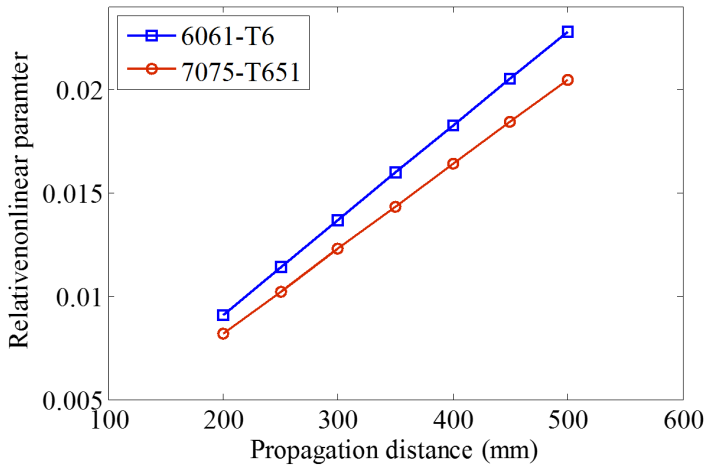

Figure 4: Relative nonlinear parameter with propagation distance

5. Three-dimensional finite element study of prestressed plate

The 3D FE study is conducted for a 500 mm × 500 mm × 2mm plate. By taking advantage of the symmetry of the problem, only a quarter of the plate is modelled using symmetry boundary and the schematic diagram is shown in Figure 5. The material properties are those of 6061-T6 aluminium alloy. The S_0 Lamb wave is excited at the corner of the model by applying 5 μm

displacement history to the nodal points at the circumference of a quarter-circle having 10 mm diameter, which represents a quarter of piezoceramic transducer. The excitation frequency of the Lamb wave in this 3D study is set at 200 kHz and the number of cycles is eight. According to the requirement for the maximum size of the element as discussed in Section 4, the in-plane element size for the 3D model is 0.4 mm and there are eight elements in the thickness direction, by which the aspect ratio of the element is 1.6. The finite elements utilised in this study are 8-noded linear brick with reduced integration (C3D8R).

Various pre-stress conditions are applied at both free boundaries with intensities σ_1 and σ_2 , where $\sigma_2 = \lambda\, \sigma_1$, and λ is the stress ratio. The pre-stress conditions are applied by adding a quasi-static loading with a duration of 0.004 sec, which is enough to avoid the transient effects of pre-stressing on the wave propagation in the next computational step. After the plate is pre-stressed, a Lamb wave is excited, and the propagating wave is measured at five different directions (θ) as illustrated in Figure 5.

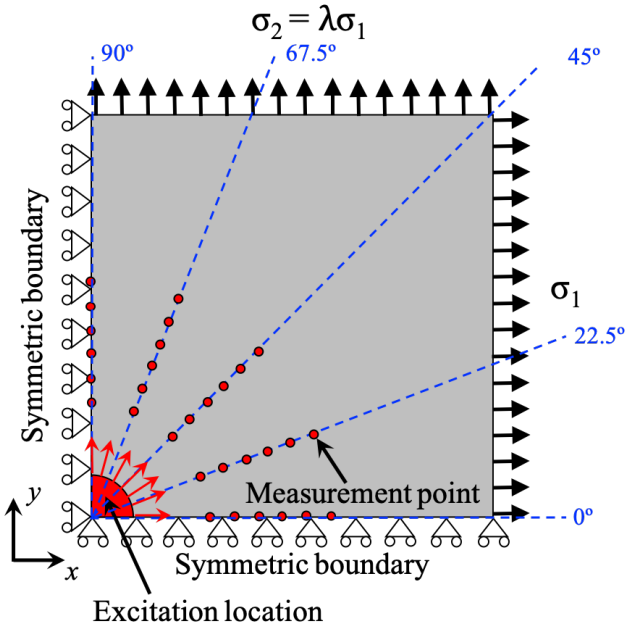

Figure 5: Schematic diagram of the 3D FE model developed in ABAQUS and positions of the measurement points

The out-of-plane strain component in the time-domain, which avoids the effect of the reflections from the FE boundaries, is obtained and transformed to the frequency-domain by fast Fourier transform (FFT). The non-linear parameter, β', is calculated using Equation (10). Figure 6 shows the variation of β' with the propagation distance ranging from 30 mm to 105 mm away from the excitation location. Figure 6 shows that for different stress ratios and propagation directions, the value of β' increases linearly with the propagation distance.

For the stress-free case and the stress ratio $\lambda = 1$ (bi-axial tension), the slopes (k) of β' versus the propagation distance diagram are the same in all propagation directions, as expected due to the symmetry of the problem. In contrast, when $\lambda = -1$ (pure shear) or 0 (uni-axial loading), the k value obtained at different propagation directions differs to each other, and the difference of k value is larger for $\lambda = -1$ than for $\lambda = 0$. For the larger stress magnitude, the rate of the growth (or the slope) of the relative non-linear parameter, β', with the propagation distance is larger as shown in Figure 7.

To compare the results for different loading conditions, a normalised slope k' is introduced, which is defined by the following equation:

$$k'(\lambda,\ \sigma_1) = \frac{k(\lambda, \sigma_1)}{k_{\text{stress free}}} \tag{11}$$

where $k_{\text{stress free}}$ is the slope of β' for the stress-free case and $k(\lambda, \sigma_1)$ is the slope for the case when the same plate is subjected to stresses defined by the pair of λ and σ_1 values.

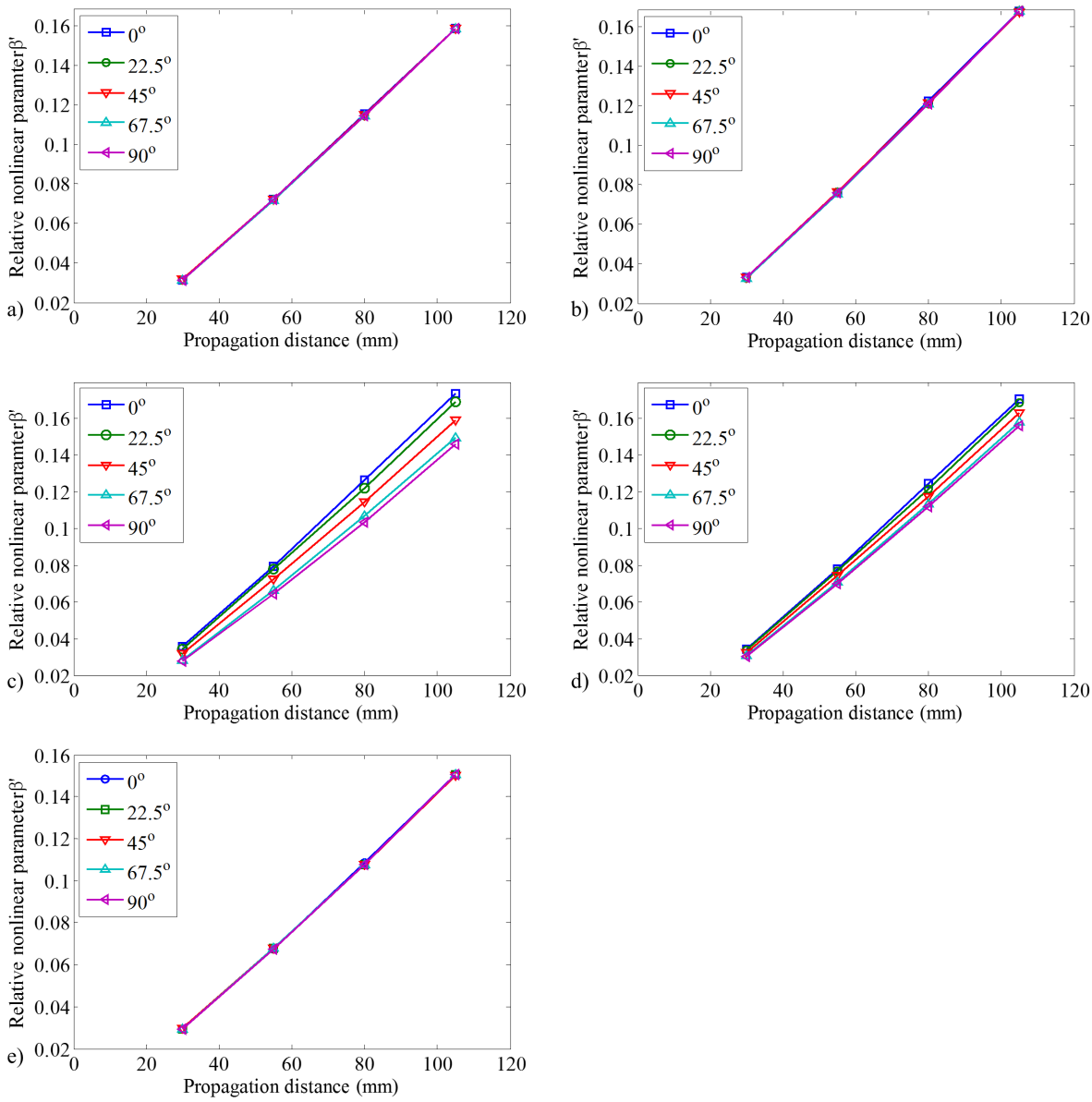

Figure 6: Relative nonlinear parameter for cases with a) stress free; b) σ1 = 100MPa, λ = 1; c) σ1 = 100MPa, λ = -1; d) σ1 = 100MPa, λ = 0; and e) σ1 = -100MPa, λ = 1 condition

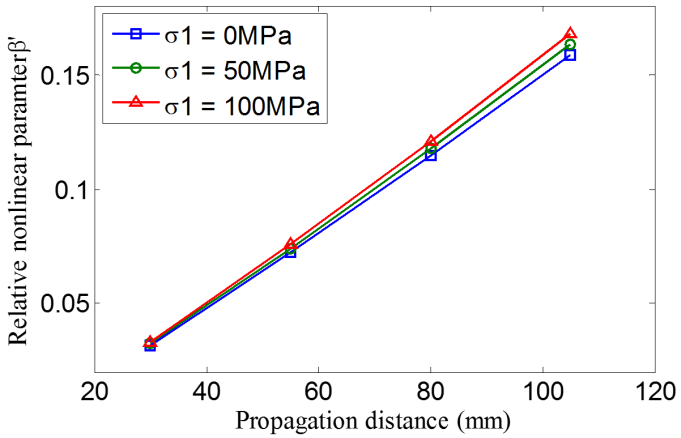

Figure 7: Relative nonlinear parameter of different stress magnitudes with propagation distance in the 45° propagation direction and λ = 1

Figure 8 shows that variation of the normalised slope, k', with the propagation distance for different pre-stressed conditions. From the figure, the results show that when $\theta \approx 22.5^{o}$, the normalised slope, k', is the same at the same magnitude of σ_1 regardless of the λ value. For the symmetric loading, i.e., $\lambda = 1$ or 0, the slope of the β' decreases when the propagation angle, θ, changes from 0^{o} to 90^{o}. It is interestingly to note that the average value of the normalised slope, k', for the pre-stress conditions of $(\lambda, \sigma_1) = (-1, 100\ \text{MPa})$ and $(1, 50\ \text{MPa})$ is the same as for $(1, 0\ \text{MPa})$ and $(0, 50\ \text{MPa})$, respectively.

In the pure shear case $(\lambda, \sigma_1) = (1, -100\ \text{MPa})$, the values of k', at different propagation directions are the same, and these values are smaller than the corresponding values for the stress-free case. In contrast, for the two bi-axial tension cases, the values of k' are larger than for the stress-free case, and the difference of the normalised slope value between stress-free and $(\lambda, \sigma_1) = (1, 100\ \text{MPa})$ cases is twice as large as the difference between the stress-free and $(\lambda, \sigma_1) = (1, 50\ \text{MPa})$ cases. Moreover, the results show that the variation of k' has the same dependency for $(\lambda, \sigma_1) = (1, 100\ \text{MPa})$ and $(\lambda, \sigma_1) = (1, -100\ \text{MPa})$. These two

pre-stress conditions have the same magnitude of stress but the first represents the bi-axial tension and the second represents a pure shear. The different patterns of the relative slope variation indicate that, generally speaking, it is possible to evaluate the stress ratios and principle stress directions in a pre-stressed plate based on the analysis of the angular variation of the non-linearity parameter, β'.

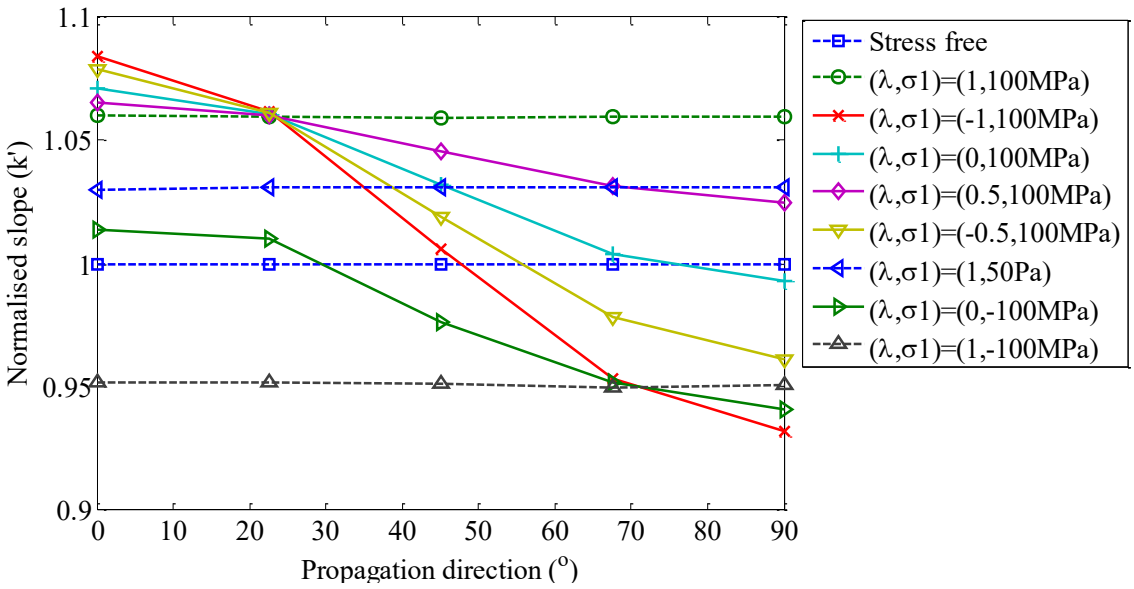

Figure 8: Variation of the normalised slope, k' with the propagation distance for different pre-stressed conditions.

6. Prestressed plate with a fatigue crack

As demonstrated in Section 5, the second-order harmonic generation could be affected by the applied stresses on structures. The tensile stress could open an initially closed fatigue crack and change the contact behaviour of the crack surface, as a consequence, the second-order harmonic generation due to contact nonlinearity could be altered and this adds difficulty in detecting the fatigue crack in the structures. In this section, the same 3D FE model used in Section 5 is employed and a fatigue crack (Figure 9) is also modelled in this 3D FE model. The second-

order harmonic generation under biaxial tension, i.e., (λ, $\sigma 1$) = (1, 100MPa), is investigated in this section.

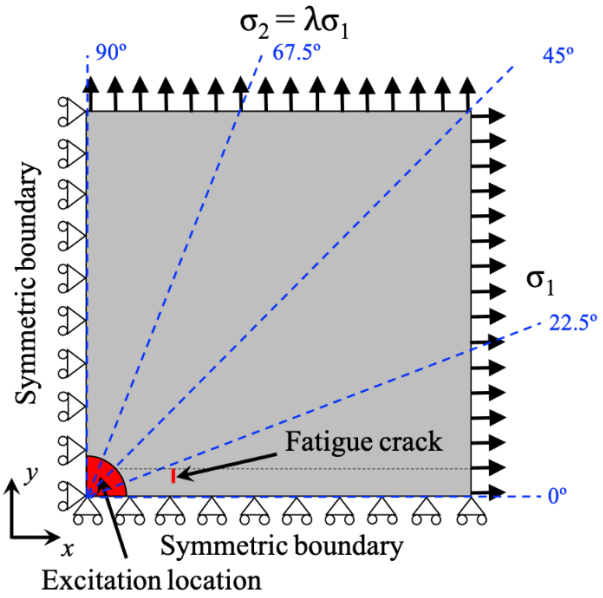

Figure 9: Schematic diagram of the 3D FE model with the fatigue crack

A 4 mm long fatigue crack located around 30 mm away from the excitation is modelled using seam in ABAQUS and the interaction and contact effect between two crack surfaces is modelled by frictional tangential contact and 'Hard' normal contact, which prevents mutual penetration of these crack surfaces. The measurements are taken at the same locations and wave propagation directions are the same as those used in Section 5. Three 3D FE models are considered, an intact plate, a plate with the fatigue crack without any applied stress, and a plate with the fatigue crack under biaxial tension. The results are compared and shown in Figure 10.

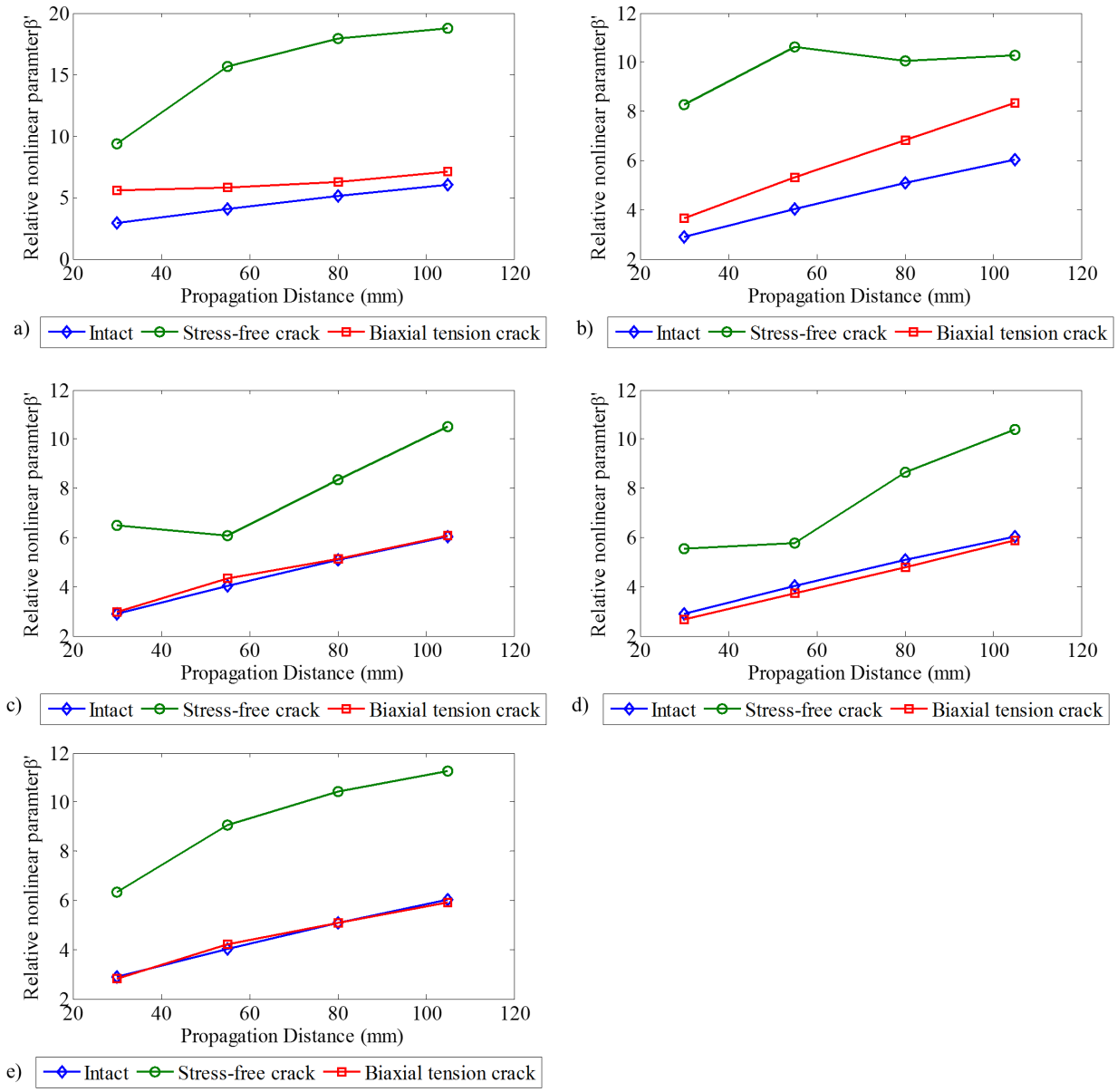

Figure 10: Relative nonlinear parameter obtained from the intact plate, unstressed, and stressed plate with the fatigue crack in a) 0°, b) 22.5°, c) 45°, d) 67.5° and e) 90° propagation directions

The results in Figure 10 show that when the fatigue crack is modelled without applying any stresses, the relative nonlinear parameter is obviously higher than that from the intact plate. It indicates that the effect of the contact nonlinearity at the fatigue crack is more dominant in

second-order harmonic generation than the intrinsic material nonlinearity. However, when the biaxial tension is applied, the β' drops to about the same level of that in the intact plate, except for the cases of 0^o and 22.5^o propagation directions with the present of the fatigue crack around these wave propagation angles. The phenomenon can be due to the fact that the fatigue crack is opened by the tensile stress, which dramatically reduces the contact area between the crack surfaces, and thus, it reduces the second-order harmonic generation due to the contact nonlinearity. This parametric study demonstrates that the second-order harmonic generation due to the fatigue crack can be overlooked if the plate is under tension, and hence, the fatigue crack is opened by tensile stress. However, it should be noted that the 3D FE model does not consider the plastic deformation around the fatigue crack, which will also generate extra second-order harmonics [49]. Further study can be conducted to confirm the reliability of second-order harmonic generation technique in detecting fatigue damage on a prestressed plate with the consideration of the plastic deformation effect.

7. Conclusions

The study has investigated the effect of the pre-stressed conditions on the generation of the second-order harmonic associated with propagation of low-frequency S_0 Lamb wave using 3D FE simulations. The material and geometric non-linearities have been modelled with the classical Murnaghan's strain energy function implemented in VUMAT subroutine of ABAQUS software package and large-strain transient FE analysis, respectively. The non-linear FE model has been extensively validated against 2D theoretical results. A good agreement between the theoretical and numerical results has been achieved with the developed FE model.

The 3D FE model of the pre-stressed plate has been modelled and the change of the rate of the accumulation of the second-order harmonic with the propagation distance has been

thoroughly investigated for different wave propagation angles (with respect to the principle stresses) and pre-stress conditions. It has been found that different pre-stress conditions have some unique features, which is potential to evaluate the stress state based on the analysis of these non-linear features. This new possibility can be important for the development of future on-line SHM systems.

The change of the non-linear parameter under the applied stress is of similar magnitude as its variation in the case of fatigue damage accumulation. As it was demonstrated in the study of Pruel *et al*. [49], the changes (increase) of the normalised non-linear parameter over the fatigue life of an aluminium plate is roughly about 10%. Referring to Figure 8, the variation of the non-linear parameter under stress can reach up to ±8%, which takes place in the pre-stress case of $(\lambda, \sigma_1) = (1, -100\ \text{MPa})$ at 0° and 90° wave propagation direction. As a result, for monitoring fatigue damage with the use of the second-order harmonic generation phenomenon it will be necessary to consider the change of the applied or residual stresses in the structural components.

Finally, the proposed 3D FE model has been used to study the stress effect on both material nonlinearity and damage detection of the plate with the fatigue crack. The results have shown that the second-order harmonic generation due to the contact nonlinearity can be overlooked if the plate is under tension and the fatigue crack is opened by the tensile stress.

8. Acknowledgement

This work was supported by the Australian Research Council (ARC) under Grant Numbers DP160102233. The support is greatly appreciated. The authors would like acknowledge Dr Munawwar Mohabuth for the discussion of implementing the non-linear constitutive equations in ABAQUS.

9. References

[1] Pan J, Zhang Z, Wu J, Ramakrishnan KR, Singh HK. A novel method of vibration modes selection for improving accuracy of frequency-based damage detection. Composites Part B: Engineering, 2019, 159:437-446.

[2] Zhang Z, Zhang C, Shankar K, Morozov EV, Singh HK, Ray T. Sensitivity analysis of inverse algorithms for damage detection in composite. Composite Structures, 2017, 176:844-859.

[3] Zhang Z, Shankar K, Morozov EV, Tahtali M. Vibration-based delamination detection in composite beams through frequency changes. Journal of Vibration and Control, 2016, 22:496-512.

[4] Bull L, Worden K, Manson G, Dervilis N. Active learning for semi-supervised structural health monitoring. Journal of Sound and Vibration, 2018, 437:373-388.

[5] Ng CT, Mohseni H, Lam HF. Debonding detection in CFRP-retrofitted reinforced concrete structures using nonlinear Rayleigh wave. Mechanical System and Signal Processing, 2019, 125:245-256.

[6] Mohseni H, Ng CT. Rayleigh wave propagation and scattering characteristics at debondings in fibre-reinforced polymer-retrofitted concrete structures. Structural Health Monitoring, 2019, 18(1):303-317.

[7] Faisal Haider F, Bhuuyan MY, Poddar B, Lin B, Giurgiutiu V. Analytical and experimental investigation of interaction of Lamb waves in stiffened aluminum plate with a horizontal crack at the root of stiffener. Journal of Sound and Vibration, 2018, 431:212-225.

[8] Ng CT. On accuracy of analytical modeling of Lamb wave scattering at delaminations in multilayered isotropic plates. International Journal of Structural Stability and Dynamics, 2015, 15(8): 1540010.

[9] Leinov E, Lowe M.J.S., Cawley P. Investigation of guided wave propagation and attenuation in pipe buried in sand. Journal of Sound and Vibration, 2015, 347: 96-114.

[10] Muggleton J.M., Kalkowski M, Gao Y, Rustighi E. A theoretical study of the fundamental torsional wave in buried pipes for pipeline condition assessment and monitoring, 2016, 374: 155-171.

[11] Yeung C, Ng CT. Time-domain spectral finite element method for analysis of torsional guided waves scattering and mode conversion by cracks in pipes. Mechanical Systems and Signal Processing, 2019, 128: 305-317.

[12] Park HW, Sohn H, Law KH, Farrar CR. Time reversal active sensing for health monitoring of a composite plate. Journal of Sound and Vibration, 2007, 302(1-2): 50-66.

[13] He S, Ng CT. A probabilistic approach for quantitative identification of multiple delaminations in laminated composite beams using guided wave. Engineering Structures, 2016, 127: 602-614.

[14] Senyurek VY, Baghalian A, Tashakori S, McDaniel D, Tansel IN. Localization of multiple defects using the compact phased array (CPA) method. Journal of Sound and Vibration, 2018, 413: 383-394.

[15] Aryan P, Kotousov A, Ng CT, Cazzolato B. A baseline-free and non-contact method for detection and imaging of structural damage using 3D laser vibrometry. Structural Control and Health Monitoring, 2017, 24(4): e1894.

[16] Zhou C, Zhang C, Su Z, Yue X, Xiang J, Li G. Health monitoring of rail structures using guided waves and three-dimensional diagnostic image. Structural Control and Health Monitoring, 2017, 24: e1966.

[17] Hughes JM, Vidler J, Ng CT, Khanna A, Mohabuth M, Rose LRF, Kotousov A. Comparative evaluation of in situ stress monitoring with Rayleigh waves. Structural Health Monitoring, 2019, 18(1): 205-215.

[18] Marzani A, Salamone S. Numerical prediction and experimental verification of temperature effect on plate waves generated and received by piezoceramic sensors, Mechanical Systems Signal Processing, 2012, 30: 204-217.

[19] Aryan P, Kotousov A, Ng CT, Wildy S. Reconstruction of baseline time-trace under changing environmental and operational conditions. Smart Materials and Structures, 2016, 25: 035018.

[20] Gandhi N, Michaels JE, Lee SJ. Acoustoelastic Lamb wave propagation in biaxially stressed plates. The Journal of the Acoustical Society of America, 2012, 132(3): 1284-1293.

[21] Mohabuth M, Kotousov A, Ng CT. Effect of uniaxial stress on the propagation of higher-order Lamb wave modes. International Journal of Non-Linear Mechanics, 2016, 86, 104-111.

[22] Mohabuth M, Kotousov A, Ng CT, Rose LRF. Implication of changing loading conditions on structural health monitoring utilizing guided wave. Smart Materials and Structures, 2018, 27: 025003.

[23] Mohabuth M, Kotousov A, Ng CT. Large acoustoelastic effect for Lamb waves propagating in an incompressible elastic plate. The Journal of the Acoustical Society of America, 2019, 145(3): 1221-1229.

[24] Packo P, Uhl T, Staszewski WJ, Leamy MJ. Amplitude-dependent Lamb wave dispersion in nonlinear plates. The Journal of the Acoustical Society of America, 2016, 140(2): 1319-1331.

[25] Yang Z., Wu Z., Zhang J., Liu K. Jiang Y., Zhou K. Acoustoelastic guided wave propagation in axial stressed arbitrary cross-section. Smart Materials and Structures, 2019, 28(4): 045013.

[26] Deng M. Cumulative second-harmonic generation of Lamb-mode propagation in a solid plate. Journal of Applied Physics, 1999, 85(6): 3051-3058.

[27] Kube CM, Arguelles AP. Ultrasonic harmonic generation from materials with up to cubic nonlinearity. The Journal of the Acoustical Society of America, 2017, 142: EL224-EL230.

[28] Soleimanpour R, Ng CT, Wang CH. Locating delaminations in laminated composite beams using nonlinear guided waves. Engineering Structures, 2017, 131: 207-219.

[29] Klepka A, Staszewski WJ, Maio DD, Scarpa F. Impact damage detection in composite chiral sandwich panels using nonlinear vibro-acoustic modulations. Smart Materials and Structures, 2013, 22: 084011.

[30] Liu P, Sohn H. Development of nonlinear spectral correlation between ultrasonic modulation components. NDT & E International, 2017, 91: 120-128.

[31] Jhang KY. Nonlinear ultrasonic techniques for non-destructive assessment of micro damage in material: A review, International Journal of Precision Engineering and Manufacturing, 2009, 10(1): 123-135.

[32] Ohara Y, Takahashi K, Ino Y, Yamanaka K, Tsuji T, Mihara T. High-selectivity imaging of closed cracks in a coarse-grained stainless steel by nonlinear ultrasonic phased array. NDT & E International, 2017, 91: 139-147.

[33] Yuan M, Zhang J, Song SJ, Kim HJ. Numerical simulation of Rayleigh wave interaction with surface closed cracks under external pressure. Wave Motion, 2015, 57: 143-153.

[34] Mohseni H, Ng CT. Higher harmonic generation of Rayleigh wave at debondings in FRP-retrofitted concrete structures. Smart Materials and Structures, 2018, 27: 105038.

[35] Mohabuth M, Khanna A, Hughes J, Vidier J, Kotousov A, Ng CT. On the determination of the third-order elastic constants of homogeneous isotropic materials utilizing Rayleigh waves. Ultrasonics, 2019, https://doi.org/10.1016/j.ultras.2019.02.006

[36] Yelve NP, Mitra M, Mujumdar PM. Detection of delamination in composite laminates using Lamb wave based nonlinear method. Composite Structures, 159(1): 257-266.

[37] Soleimanpour R, Ng CT, Wang CH. Higher harmonic generation of guided waves at delaminations in laminated composite beams. Structural Health Monitoring, 2017, 16(4): 400-417.

[38] Liu X, Bo L, Yang K, Liu Y, Zhao Y, Zhang J, Hu N, Deng M. Locating and imaging contact delamination based on chaotic detection of nonlinear Lamb waves. Mechanical Systems and Signal Processing, 2018, 109: 58-73.

[39] He S, Ng CT. Modelling and analysis of nonlinear guided waves interaction at a breathing crack using time-domain spectral finite element method. Smart Materials and Structures, 2017, 26: 085002.

[40] Shen Y, Wang J, Xu W. Nonlinear features of guided wave scattering from rivet hole nucleated fatigue cracks considering the rough contact surface condition. Smart Materials and Structures, 2018, 27: 105044.

[41] Yang Y, Ng CT, Kotousov A. Influence of crack opening and incident wave angle on second harmonic generation of Lamb waves. Smart Materials and Structures, 2018, 27: 055013.

[42] Scarselli G, Ciampa F, Ginzburg D, Meo M. Non-destructive testing techniques based on nonlinear methods for assessment of debonding in single lap joints. SPIE Proceedings, 2015, 9437: 943706.

[43] Mandal DD, Banerjee S. Identification of breathing type disbonds in stiffened panel using non-linear lamb waves and built-in circular PWT array. Mechanical Systems and Signal Processing, 2019, 117: 33-51.

[44] Amerini F, Meo M. Structural health monitoring of bolted joints using linear and nonlinear acoustic/ultrasound methods. Structural Health Monitoring, 2011, 10(6): 659-672.

[45] Yang Y, Ng CT, Kotousov A. Bolted joint integrity monitoring with second harmonic generated by guided waves. Structural Health Monitoring, 2019, 18(1):193-204.

[46] Kube CM, Turner JA. Acoustic nonlinearity parameters for transversely isotropic polycrystalline materials. The Journal of the Acoustical Society of America, 2015, 137: 3272-3280.

[47] Chillara VC, Lissenden CJ. Review of nonlinear ultrasonic guided wave nondestructive evaluation: theory, numerics, experiments. Optical Engineering, 2016, 55(1): 011002.

[48] Wan X, Tse PW, Xu GH, Tao TF, Zhang Q. Analytical and numerical studies of approximate phase velocity matching based nonlinear S_0 mode Lamb waves for the detection of evenly distributed microstructural changes. Smart Materials and Structures, 2016, 25:045023.

[49] Pruell C, Kim JY, Qu J, Jacobs LJ. A nonlinear-guided wave technique for evaluating plasticity-driven material damage in a metal plate. NDT & E International, 2009, 42: 199-203.

[50] Kim JY, Jacobs LJ, Qu J. Experimental characterization of fatigue damage in nickel-base superalloy using nonlinear ultrasonic waves. Journal of Acoustical Society of America, 2006, 120(3): 1266-1273.

[51] Hong M, Su Z, Wang Q, Cheng L, Qing X. Modelling nonlinearities of ultrasonic waves for fatigue damage characterization: Theory, simulation, and experimental validation. Ultrasonics, 2014, 54: 770-778.c

[52] Müller MF, Kim JY, Qu J, Jacobs LJ. Characteristics of second harmonic generation of Lamb waves in nonlinear elastic plates. Journal of Acoustical Society of America, 2010, 127(4): 2141-2152

[53] Matlack KH, Kim JY, Jacobs LJ, Qu J. Experimental characterization of efficient second harmonic generation of Lamb wave modes in a nonlinear elastic isotropic plate. Journal of Applied Physics, 2011, 109(1): 014905

[54] Sohn H. Reference-free crack detection under varying temperature. KSCE Journal of Civil Engineering, 2011, 15(8): 1395-1404.

[55] Nucera C, Lanza di Scalea F. Monitoring load levels in multi-wire strands by nonlinear ultrasonic waves. Structural Health Monitoring, 2011, 10(6): 617-629.

[56] Pau A, Lanza di Scalea F. Nonlinear guided wave propagation in prestressed plates. The Journal of the Acoustical Society of America, 2015, 137(3): 1529-1540.

[57] Murnaghan FD. Finite deformation of an elastic solid. American Journal of Mathematics, 1937, 59(2): 235-260.